Bedford, J., Moreno, M., Schurr, B., Bartsch, M., Oncken, O. (2015): Investigating the final seismic swarm before the Iquique-Pisagua 2014 M w 8.1 by comparison of continuous GPS and seismic foreshock data. - *Geophysical Research Letters*, *42*, 10, p. 3820-3828.

DOI: http://doi.org/10.1002/2015GL063953

AGU PUBLICATIONS

Geophysical Research Letters

RESEARCH LETTER
10.1002/2015GL063953

Key Points:
- cGPS transient signals due to slip and afterslip of foreshock sequence
- Probable positions of cGPS calculated from uncertainties in source parameters
- 16 March M_w 6.7 strike is rotated considerably from the plate interface strike

Supporting Information:
- Text S1, Figures S1–S13, Table S1, and Captions of Data Sets S1–S3 and Movies S1–S6
- Data Set S1a
- Data Set S1b
- Data Set S1c
- Data Set S1d
- Data Set S1e
- Data Set S2a
- Data Set S2b
- Data Set S2c
- Data Set S2d
- Data Set S2e
- Data Set S3a
- Data Set S3b
- Data Set S3c
- Data Set S3d
- Data Set S3e
- Movie S1
- Movie S2
- Movie S3
- Movie S4
- Movie S5
- Movie S6

Correspondence to:
J. Bedford,
jbed@gfz-potsdam.de

Citation:
Bedford, J., M. Moreno, B. Schurr, M. Bartsch, and O. Oncken (2015), Investigating the final seismic swarm before the Iquique-Pisagua 2014 M_w 8.1 by comparison of continuous GPS and seismic foreshock data, *Geophys. Res. Lett.*, *42*, 3820–3828, doi:10.1002/2015GL063953.

Received 23 MAR 2015
Accepted 1 MAY 2015
Accepted article online 6 MAY 2015
Published online 23 MAY 2015

Investigating the final seismic swarm before the Iquique-Pisagua 2014 M_w 8.1 by comparison of continuous GPS and seismic foreshock data

Jonathan Bedford[1], Marcos Moreno[1], Bernd Schurr[1], Mitja Bartsch[1], and Onno Oncken[1]

[1]Deutsches GeoForschungsZentrum, Telegrafenberg, Potsdam, Germany

Abstract Preexisting networks of seismometers and continuous GPS in Northern Chile successfully captured surface motions and seismicity leading up to the 1 April M_w 8.1. Here we compare continuous GPS (cGPS) with predictions of seismic dislocations for the final foreshock swarm, beginning with the 16 March M_w 6.7. Results show that the cumulative cGPS motion can be largely explained by seismic slip because evolutions of cGPS positions for most stations stay within the ranges of seismic predictions (given sensible ranges of assumed source errors). However, cGPS motions between 18–21 and 25–31 March outpace seismic predictions, supporting the existence of aseismic transients that were most probably the afterslip from preceding bursts of seismicity. A parameter search reveals that the 16 March M_w 6.7 cGPS displacements can be recreated with a fault plane significantly rotated anticlockwise from the strike of the plate interface, suggesting that failure was on a structure other than the plate interface.

1. Introduction

The M_w 8.1 Iquique-Pisagua earthquake of 1 April 2014 was exceptionally well monitored by the Integrated Plate Boundary Observatory Chile (IPOC: www.ipoc-network.org) with various geophysical instrumentations already in place due to the expected failure of a mature seismic gap on the Andean subduction margin [*Comte and Pardo*, 1991; *Chlieh et al.*, 2011]. This earthquake ruptured only a small portion of this seismic gap leaving a remaining slip deficit to potentially harbor an earthquake of $Mw > 8.9$ [*Schurr et al.*, 2014]. Of particular interest to the community researching, this margin is the occurrence of foreshock clusters in the year leading up to the main shock, with the ultimate and most active cluster lasting from 16 March (when it was initiated by a M_w 6.7) until the onset of the main shock (Figure 1). This final foreshock cluster was accompanied by a transient continental surface deformation recorded on land by the IPOC continuous GPS (cGPS) network [*Schurr et al.*, 2014; *Ruiz et al.*, 2014]. Hence, the spatial-temporal pattern of seismicity and deformation leading up to the Iquique-Pisagua earthquake is of particular interest regarding precursory activity and may provide insights for improving earthquake hazard assessment based on future margin activity.

There currently exists some discord as to whether the transient deformation recorded by the continuous GPS (cGPS) can be explained by seismic or aseismic slip of the plate interface. Some studies have suggested slow slip as a significant tectonic process during the final foreshock cluster, with evidence presented from either cGPS records [*Ruiz et al.*, 2014] or the recognition of repeating earthquakes [*Kato and Nakagawa*, 2014; *Meng et al.*, 2015]. By contrast, the cumulative preseismic GPS displacements have been reproduced with predicted earthquake slip based on location, mechanism, and magnitude from scaling relations [*Schurr et al.*, 2014]; in this case the centroid of slip for each event was assumed to be at the hypocenter (from the catalog produced by GEOFON (geofon.gfz-potsdam.de)), and the failure directions of all events were assumed to be opposite to the azimuth of plate convergence, the latter obviously not always being true. Particularly as the largest foreshock (M_w 6.7) apparently was not on the plate interface [*Schurr et al.*, 2014; *Hayes et al.*, 2014] but was modeled as such by *Schurr et al.* [2014] when predicting its deformation. The M_w 6.7 foreshock is suspected to have occurred in the upper plate, due to the peculiar rotation of the shallowest nodal plane of the focal mechanism with respect to the slab geometry [*Hayes et al.*, 2014], although there is some variability in the moment tensor solutions (Table S1 in the supporting information) leading to some uncertainties in the most likely location and tectonics of this event.

The primary aim of this study is to contribute to the discussion concerning competing hypotheses of aseismic and seismic failure during the final 16 days leading to the earthquake. This will be achieved by producing a

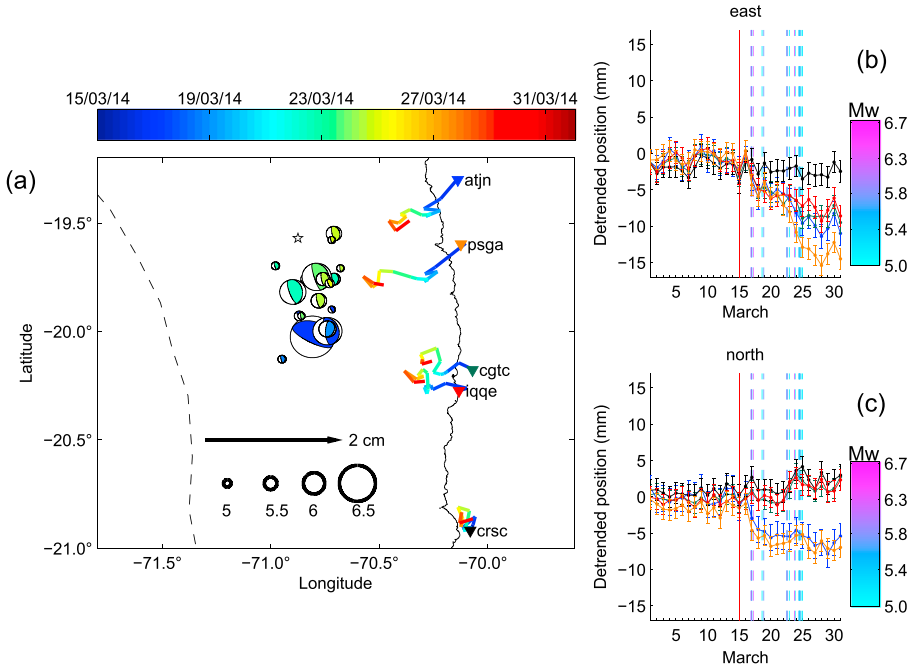

Figure 1. (a) Map view of the subduction zone. Dashed black line represents the subduction trench, and solid black line is the coastline of Chile. Small white star is the location of the 1 April 2014 M_w 8.1 epicenter. Focal mechanisms (geofon.gfz-potsdam.de) shown are for the foreshock sequence beginning on 16 March and are chronologically color coded, corresponding to the color bar above. Size of plotted focal mechanisms corresponds to the magnitudes shown by the radii of the black circles, and these sizes correspond to the extents of the event if it were to fail in a circular pattern. Stations of interest in the analyses of seismic motion are shown on the plot as colored triangles. The colors of these triangles correspond to the colors shown in Figures 1b and 1c. The colored lines originating from the station locations represent the time evolutions of transient motion (available for download in the supporting information) and are color coded in the same way as the focal mechanisms. (b) Plot of the March 2014 eastward deformation at the cGPS locations shown in Figure 1a. Colors correspond to the colors of the triangular station markers in Figure 1a. (c) Same as Figure 1b but for the north component. Data shown in Figures 1b and 1c have been detrended, and common mode filtered.

range of time-dependent predicted positions for the cGPS by considering the errors in the seismic catalog. This approach allows for the respective evolutions of actual and predicted positions to be compared while also considering the errors in both data and prediction domains. To investigate the seismic efficiency of the slip leading up to the Iquique-Pisagua earthquake, we will analyze the evolution of the surface deformation predictions at the cGPS locations modeled from the dislocations of the foreshock events. We focus on the progression of 16 days before the main shock. For each event in the foreshock catalog we consider a sensible range of errors in the focal mechanisms and hypocentral locations to produce probability density functions (PDFs) of predicted displacement at each cGPS location. These PDFs are transformed into the temporal format of the daily cGPS data so that the transient behavior of data and predictions can be compared on a daily basis. Additionally, the methodology for predicting seismic displacements is reversed to conduct a parameter search for the M_w 6.7 foreshock of 16 March with the aim of constraining the focal mechanism of this event. Finally we interpret the results in the framework of the known plate kinematics that have been monitored at this segment.

2. Methods

2.1. Modeling Seismic Predictions

We model surface predictions of deformation using analytical solutions for dislocations in an elastic half-space [*Okada,* 1985], with the elastic parameters $G = 3.5E9$ Pa and Poisson's ratio = 0.25 deduced from seismic tomography and gravity studies [*Husen et al.*, 2000; *Tassara and Echaurren,* 2012]. For all events considered by our forward modeling we set the length and width of each rectangular source according to the scaling relations between seismic magnitude and source dimensions in subduction zones [*Strasser et al.,* 2010]. The

parameters varied for each event are the hypocentral location (x, y, z), strike, dip, slip azimuth, and magnitude of uniform slip. The strike, dip, and slip azimuth for each event are taken from published focal mechanisms (see supporting information). Slip azimuth comes from the horizontal component of the slip vector given by equations (1)–(3) [*Aki and Richards,* 2002] applied to the strike, dip, and rake of the focal plane:

$$\text{north} = \cos(\text{rake}) \times \cos(\text{strike}) + \cos(\text{dip}) \times \sin(\text{rake}) \times \sin(\text{strike}), \quad (1)$$

$$\text{east} = \cos(\text{rake}) \times \sin(\text{strike}) - \cos(\text{dip}) \times \sin(\text{rake}) \times \cos(\text{strike}), \text{and} \quad (2)$$

$$z = -\sin(\text{rake}) \times \sin(\text{dip}). \quad (3)$$

The uniform slip magnitude for each event satisfies the equation from *Brune* [1968]:

$$M_0 = \mu \cdot A \cdot D, \quad (4)$$

where M_0 is the known seismic moment, μ is shear modulus of the elastic medium in the vicinity of the slipping region, A is the assumed area of the source region (already defined by seismic scaling relations), and D is the uniform slip magnitude. Since there is some uncertainty of the shear modulus value and its heterogeneity at the plate interface we calculate a probability distribution of μ using randomly selected combinations of parameters from a range of Chilean subduction plate interface densities (2700–3000 kg m^{-3}), V_p wave speeds (6250–7000 m s^{-1}), and V_p to V_s ratios (1.8–2.0) [*Tassara and Echaurren,* 2012; *Husen et al.*, 2000; *Hicks et al.*, 2012]. Therefore, our modeling approach assumes a single shear modulus, G, of 35 GPa for the calculation of surface motions due to elastic dislocations, and a lognormal probability distribution of shear moduli, μ, at the plate interface between 28 and 44 GPa (see supporting information and Figure S1) which are solely used to calculate the range and a priori probability distribution of uniform slip for each modeled event. The sensitivity of the Greens functions to the uncertainty of the Poisson's ratio and shear modulus (G) for the elastic half-space is negligible, and so we do not include this variability in our forward modeling.

For the forward modeling of seismic predictions of the foreshock sequence, strike, dip, and slip azimuths are varied ±15°, ±10°, and ±15°, respectively, from the central values derived from focal mechanisms. Hypocenters are varied ±15 km, ±15 km, and ±10 km in the east, north, and vertical directions, respectively. This variability in source parameters is in keeping with the variation observed in available focal mechanisms and hypocenters from various sources (e.g., Table S1).

For the M_w 6.7 parameter search, the parameter space is sampled more finely and with a wider range of variability in all parameters. Strike, dip, and slip azimuths are varied between −135° and 45° for strike, between 4° and 25° for dip, and between −200° and 20° for slip azimuth. The hypocenter is varied ±20 km in both east and north directions and between 5 and 25 km in depth. Due to computational speed, we do not vary slip magnitude in the M_w 6.7 parameter search, assuming slip of all parameter combinations to be in agreement with the mean value of the μ distribution, 35 GPa. The average of the best solutions for the M_w 6.7 is then assumed for the default parameters for this event in the modeling of the evolution of seismic predictions of the whole foreshock series. We neglect events with a magnitude of less than M_w 5 since we generally did not have focal mechanisms for these events.

2.2. GPS Data

Figures 1b and 1c show the detrended daily solutions at the cGPS stations closest to the foreshock activity. A common mode filter (supporting information) has been applied to this data to remove network-correlated noise [*Wdowinski et al.*, 1997]. The zero positions of the data are assigned as the mean north and east station positions of the detrended data between 1 and 15 March 2014. Since there is no significant transient deformation apparent in the cGPS and no significant seismic activity between 1 and 15 March, we can evaluate the noise in the signal during this epoch. Consequently, errors at each station are defined by the standard deviations of the east and north components in this time period.

For the parameter search of the 16 March M_w 6.7 we fit the displacement obtained by the cGPS between 15 and 17 March. This is due to the daily format of the cGPS solutions. The daily position of the GPS is the mean position, and the M_w 6.7 occurred late in the day, meaning that the cumulative displacement of this event is more apparent in the cGPS positions on the following day, 17 March. There is some contamination of the fitted signal by a subsequent M_w 6.3 on the 17 March contributing in total to 20% of moment release (M_0 release) captured in this epoch; therefore, we removed the prediction of this event from the displacements of this epoch

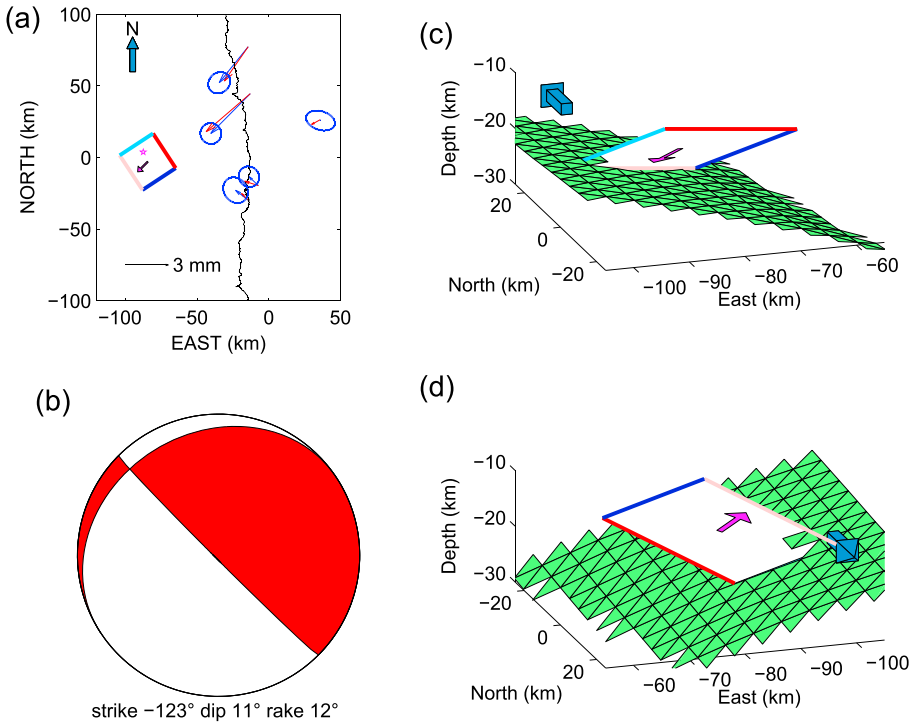

Figure 2. (a) Plan view of the GPS data and predictions for the average solution of the parameter search for the 16 March M_w 6.7. Blue vectors and ellipses represent the data displacements estimations for this event with 67% confidence. Red vectors are the predictions. Black line represents the Chile coastline. Average of the best fitting fault planes is shown along with a failure vector plotted from the center (centroid) of the fault plane. Colors of each side of the fault plane are repeated in Figures 2c and 2d. Plot is in Cartesian coordinate system with origin at 70°W and 20°S. Magenta star is the epicenter from the GEOFON regional waves seismic solution (Table S1). (b) Focal mechanism of the average of the best fitting fault planes of the parameter search. (c) Average fault plane plotted with the Slab 1.0 plate interface in green [*Hayes et al.*, 2012] from a south-westerly look angle. North arrow is plotted to help clarify the look angle. Fault plane is plotted as a mesh of green triangles. (d) Same as Figure 2c but from a north-east look angle.

(supporting information). The predictions of lower magnitude events during this epoch were not subtracted because they were negligible in magnitude in comparison to those of the M_w 6.7 and M_w 6.3.

2.3. cGPS Predictions: Probability Density Functions

The suite of cGPS displacement predictions for each event in the foreshock series is sampled into a probability density function in the east and north prediction manifold. These PDFs are then chronologically cascaded so that for each consecutive event, the PDF is added X amount times the positions of the prior PDF, with X depending on the PDF value at each particular position of the prior PDF (for more details and discussion of this method, see supporting information). After the PDFs have been cascaded, we obtain a daily PDF for each day of the foreshock series by sampling and appropriately weighting the cascaded PDFs according to the time that each event occurred on the particular day. For the daily PDF calculation, a point from each cascaded PDF is sampled randomly before a new point is calculated by weighting the sampled points by the fraction of the day that each event has been representative of that day's cumulative seismic motion. This creation of new points by random sampling and time weighting is repeated until we have a new cloud of points thereby creating a daily PDF.

3. Results

3.1. Parameter Search for the Source Characteristics of the 16 March M_w 6.7

The best fitting solutions are defined by those solutions that produce predictions within the error ellipses of the data at one standard deviation. Figures 2a, 2c, and 2d show the mean parameters of all the best fitting models found in the parameter search. This average model represented by the mean of each best fitting

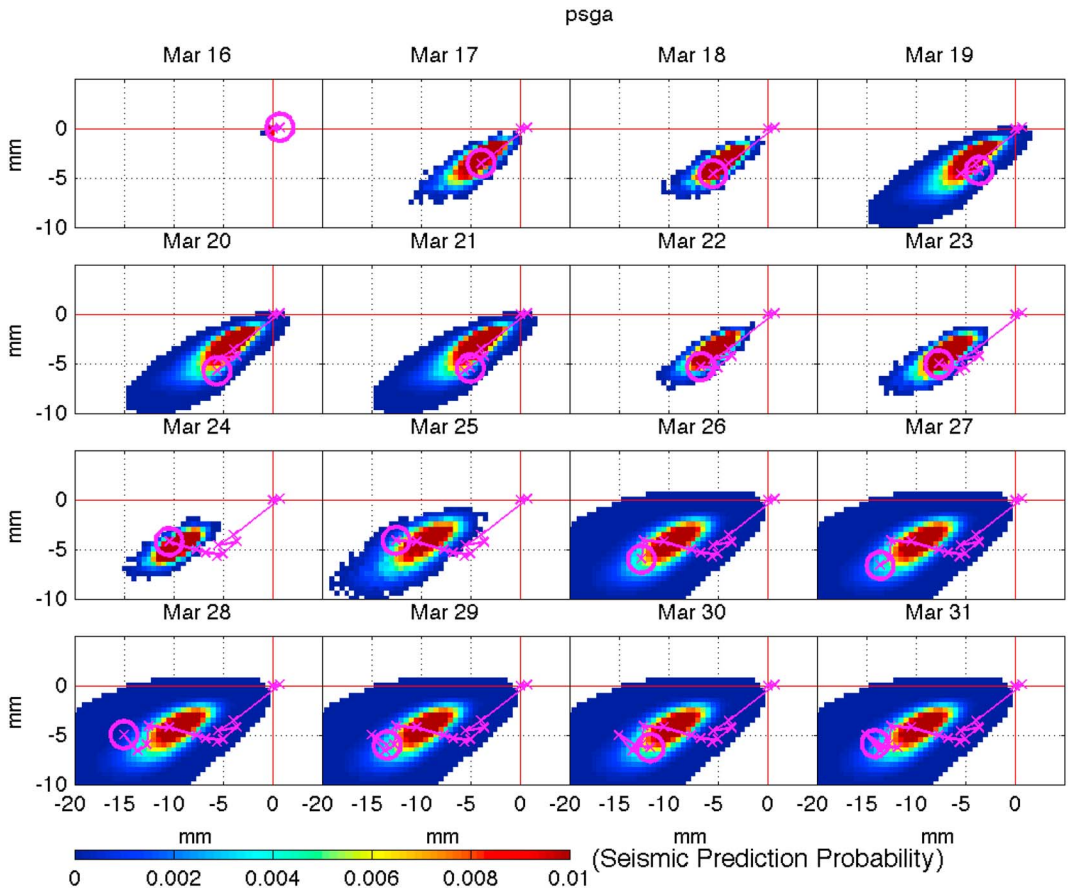

Figure 3. Chronological evolution of the seismic predictions of station position and the actual station position from cGPS for psga. Time increase is given by the data above each panel. *X* and *Y* axes correspond to east and north motion. Colors represent the probability distribution of the seismically predicted station position. The growing magenta line represents the cumulative cGPS data motion, and the ellipse at the end of this line represents the 95% error range of this cumulative displacement. At this particular station we see that the most probable predicted positions of the cGPS follow the data, with perhaps the data growing at a slightly greater rate than the range of most likely predictions.

parameter has a strike of −123°, dip of 11°, and a rake of 12°, giving a slip azimuth roughly in line with the direction of plate convergence. The centroid of the average model lies in the upper plate, although the centroid location of best fitting solutions can vary significantly, to a similar order of that of the seismically determined centroids (the maximum distance between best fitting centroids of the parameter search being 26 km and the largest distance between seismic centroids being 21 km). The centroid locations of the parameter search are in the vicinity of the range of centroids from seismic estimations (Figure S5). The average fault plane dips to the northwest, and the focal mechanism for failure on such an oriented fault would be a highly oblique thrust (Figure 2b). Figure S6 shows the variability of the strikes, dips, and rakes of the various planes that fit the data. The strikes of the best fitting planes vary between −90° and −135°, dip is constrained between 5° and 17.5°, and slip azimuth is constrained between 215° and 270°. Figure S7 shows the best fitting suite of focal mechanisms output by the parameter search, and Figure S8 compares the mean solution to the seismically determined focal mechanisms. We find that the mean fault plane solution is most similar to that of the U.S. Geological Survey using body waves (earthquakes.usgs.gov).

3.2. Foreshock Sequence

Figure 3 shows an example of the comparison between seismic prediction evolution and GPS data evolution for the station psga (Movies S1–S5 and Figures S9–S13 show these comparisons for all stations used in the analysis). At psga, the data position and its associated uncertainty ellipse stays within the most likely predicted positions as both the mean data and prediction positions move toward the epicenters of the

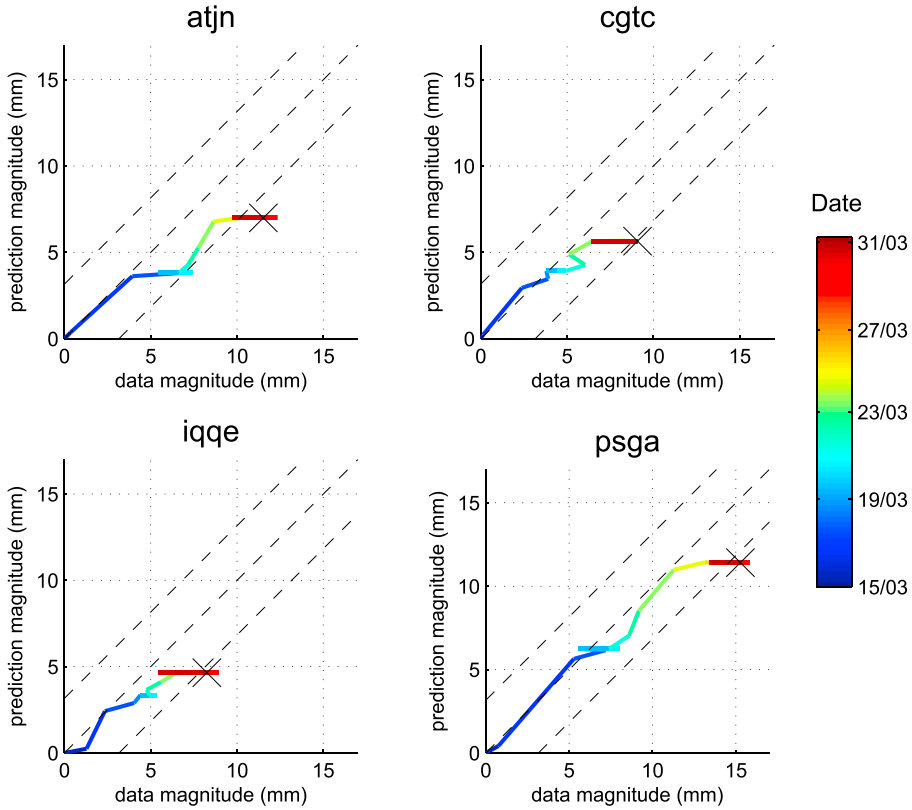

Figure 4. Cross plots of the cumulative mean data magnitudes and mean prediction magnitudes are shown on each panel, with the time corresponding to the location on the cross plot given by the color bar. Dashed black lines represent a gradient of 1. At stations atjn and psga we see most clearly two decreases in gradient, suggesting two times when the cGPS motion was not seismically explained, most probably due to aseismic afterslip following the preceding bursts of foreshock activity. At all stations the days from 25 March onward are characterized by a horizontal motion in the cross plots partially due to noise and partially suspected to be aseismic motion (see Movie S6). Final mean magnitudes on 31 March are plotted with a black cross.

foreshock clusters with time (Movie S5). At the other stations we see this spatiotemporal overlap between data uncertainty and prediction range, except for the northernmost station atjn where we see a divergence in time between data uncertainty and prediction range (Figure S9).

Since the data generally stays within the bounds of the most likely locations predicted by forward modeling of seismic sources, it can be stated that the cumulative surface deformation of these stations can be, with the exception of atjn, explained by the surface displacements associated to the cluster of seismic events. Of course this statement is subject to the consideration of the assumed errors in the seismic source parameters: Naturally, wider and narrower ranges of input variability in the seismic parameters would result in a broadened and restricted region of predicted cGPS position in the PDF, respectively, meaning that the cGPS motions fall within the range of seismic predictions if the ranges of input parameters for each event are wide enough.

Another pertinent comparison to make between data and prediction is the comparison of the rate of change in displacement magnitude. Figure 4 shows the evolution of total displacement magnitude for both predictions and data for the common mode-filtered data. In this analysis we are interested in the gradient of the cross-plotted rates of data and prediction magnitude: the greater the gradient decrease from 1, the more likely that the motion of the GPS station is explained by aseismic activity (assuming that all other seismic activity that is neglected by our event magnitude cutoff is not responsible for the extra GPS motion). An overprediction of GPS motion would result in a gradient greater than 1. Since we do not see significant displacement in either prediction or data at the station crsc, we neglect this station for this analysis. At the four closest stations cgtc, iqqe, and psga, and atjn we see an initial gradient of slightly less

than 1 indicating an in-concert evolution between mean prediction and data positions. Between the times of 18–21 March we suspect aseismic motion most strongly at atjn and slightly at psga. All stations exhibit some noise at the end of the time series from 25 March onward and that manifests itself as a horizontal right-to-left motion on the cross plots (as the noise occurs and corrects itself). However, despite this noise, there is an indication that aseismic motion has occurred some time between 25 and 31 March at all stations due to the pronounced flattening of the gradient in all the cross plots during this period.

In summary, we can state that the cumulative motion of the surface matches the cumulative motion of the most probable predicted positions within the assumed error distribution of source parameters for all stations except atjn. However, this statement is subject to the confidence in our assumed errors in our input source parameters. Furthermore, the magnitude of the mean data predicted position initially increases at a similar rate before the data outpaces the predictions at two stations between 18 and 21 March and at all stations on or after 25 March, suggesting the detection of two aseismic slip transients.

4. Discussion

The results of the parameter search and forward modeling approaches presented in this study must be considered within the limitations of the assumptions made in the modeling. While we can estimate the bounds of error for input parameters using the variability found in independently obtained seismic hypocentral locations and focal mechanism solutions, it is unknown what kind of probability distribution these codependent errors should take. Sources of these errors come from oversimplified velocity models used in hypocentral and moment tensor inversions, noise in the seismic data, as well as artifacts introduced by the processing of moment tensor solutions. An example of the variability of a seismic event is found by comparing independently derived solutions from the M_w 6.7 foreshock (Table S1 and Figure S8). Nevertheless, even with conservative estimates of source parameter errors we can state that the cumulative transient in the data is mostly explained by the cumulative displacement along the plate interface from the foreshocks. Only at the northernmost station (atjn) do we see an evolution of cGPS position that exceeds the range of most probable predicted positions.

Given that the modeled seismic slip can reproduce most of the cumulative signal in the data within given error considerations, we must then ask what spatiotemporal role that the aseismic slip plays during the foreshock sequence. Certainly, the outpacing of the data over the prediction in mean magnitude evolution, evident both between 18 and 21 March and following 25 March leading to the main shock on 1 April, strongly suggests the occurrence of aseismic slip. However, the increased noise levels in the data concurrent with this suspected aseismic motion in the final week leading to the main shock slightly decreases our confidence in occurrence of the second transient.

Detection of repeating events [*Kato and Nakagawa*, 2014; *Meng et al.*, 2015] has been taken as an additional indication of slow slip. However, neither these repeating events nor indeed the microseismicity have occurred with a high enough frequency or regularity during the final 16 days leading to the M_w 8.1 main shock to support the case of a background slow slip forcing seismicity. Furthermore, it remains to be demonstrated whether these repeating events did indeed break the exact same patches, based on the source dimensions and location uncertainties. Even if the repeating events have occurred on the same patches, forcing mechanisms other than slow slip (for instance, fluid pressure change) could explain the seismicity. Therefore, the proposed slow slip associated with the repeating events may have occurred, but this slow slip is certainly not the main process contributing to the transient cGPS motion captured during this final foreshock sequence beginning on 16 March. If such a slow slip has occurred concurrent with repeating events, then the surface signal is not detectable above the level of data noise. Moreover, the aseismic deformation transients that we have detected are not strongly correlated in time to the repeating events. Figure 1 shows how the largest events occur in two bursts, the first southerly sequence occurring between 16 and 18 March and the second northerly sequence occurring between 22 and 25 March. Indeed, the identification of aseismic motion following both of these seismic bursts strongly supports the scenario of a postseismic response to foreshocks, most likely in the form of aseismic afterslip. The time series are too noisy to provide a reliable inverted location of aseismic slip, although the difference in mean data and prediction displacements leaves a signal that generally points toward the location of the foreshock activity.

The M_w 6.7 of 16 March is seen as the point at which the foreshock series intensified, and therefore, its source parameters are of particular interest in trying to understand the runaway process leading up to the main shock. From the results of our parameter search, we show that the final foreshock sequence was triggered by a fault plane striking between −135° and −90°. This result is significant in that it indicates a failure on a plane other than the megathrust, which would have a more northerly rotated strike. For other parameters of the parameter search (hypocentral location, dip, and rake) we do not see an improvement in constraint compared to those given by initial seismic estimations. Therefore, while our method indicates failure on an unconventional fault plane, it does not show if such fault plane is in contact with the plate interface or is sitting higher in the upper crust.

The significance of an intraplate M_w 6.7 in facilitating this accelerated unlocking of the interface remains unclear: If this event had happened on the plate interface, then the subsequent foreshock series may still have resulted in the final rupture of the M_w 8.1. If the location and mechanism of the M_w 6.7 fault is significant, then we could speculate that this event allowed the release and migration of upper plate fluids onto the plate interface. In this scenario, an increase fluid pressure on the plate interface would reduce the effective normal stress and thereby promoting a decrease of the locking degree [*Audet and Schwartz*, 2013; *Moreno et al.*, 2014]. In an alternative scenario, an increase in permeability in the vicinity of the M_w 6.7 rupture could have drawn fluids away from the plate interface, thereby strengthening the interface and pushing it into a state more susceptible to rate weakening and therefore seismic failure.

5. Conclusions

This study has shown that the transient signal in cGPS data following and including the 16 March M_w 6.7 foreshock leading up to the M_w 8.1 main shock of 1 April can be largely explained by seismic slip, given a realistic range of foreshock source parameter uncertainties. With the exception of the northernmost station, atjn, and with the consideration of noise, the evolution of a transient signal in the data does not fall outside of the bounds of the probable seismic prediction locations, although the time-dependent rates of mean data and prediction magnitude evolution have revealed possible periods of aseismic motion between 18 and 21 March and between 25 and 31 March. Due to noise levels in the data we cannot rule out the possibility of a very low rate background aseismic slip that could be forcing the seismicity and repeating events. However, the aseismic slip that we can detect is most likely to be a response to the foreshocks in the form of afterslip.

The methods demonstrated in this paper have a strong potential to be applied to other scenarios where there exists both dense cGPS and seismometer networks to identify the contribution of seismic displacements to the transient signals recorded in the GPS. Improvement of the forward modeling of seismic prediction PDFs could be obtained by improving our knowledge of the a priori probability distributions of the seismically obtained parameters. By comparing the seismically obtained parameters of the 16 March M_w 6.7 to that of our parameter search, we see that the GPS displacements better constrain the strike of the event, although constraints on hypocentral location, dip, and azimuth of seismic failure are not improved.

Acknowledgments

We are grateful for the funding provided by the German Research Foundation (DFG) for MARISCOS project MO/2310/1-1. Continuous GPS data are freely shared between the IPOC partners, and we are grateful to our international partners for their efforts in maintaining the network. The processed time series presented by this paper can be downloaded from the supporting information. We would like to thank the two anonymous reviewers for their insightful comments, which have ultimately improved the discussion and interpretation of our results [Simons *et al.*, 2010].

The Editor thanks two anonymous reviewers for their assistance in evaluating this paper.

References

Aki, K., and P. G. Richards (2002), *Quantitative Seismology*, vol. 1, Univ. Science Books, Sausalito, Calif.

Audet, P., and S. Schwartz (2013), Hydrologic control of forearc strength and seismicity in the Costa Rican subduction zone, *Nat. Geosci.*, *6*, 852–855.

Brune, J. N. (1968), Seismic moment, seismicity, and rate of slip along major fault zones, *J. Geophys. Res.*, *73*(2), 777–784, doi:10.1029/JB073i002p00777.

Chlieh, M., H. Perfettini, H. Tavera, J.-P. Avouac, D. Remy, J.-M. Nocquet, F. Rolandone, F. Bondoux, G. Gabalda, and S. Bonvalot (2011), Interseismic coupling and seismic potential along the Central Andes subduction zone, *J. Geophys. Res.*, *116*, B12405, doi:10.1029/2010JB008166.

Comte, D., and M. Pardo (1991), Reappraisal of great historical earthquakes in the northern Chile and southern Peru seismic gaps, *Nat. Hazards*, *4*, 23–44.

Hayes, G. P., D. J. Wald, and R. L. Johnson (2012), Slab1. 0: A three-dimensional model of global subduction zone geometries, *J. Geophys. Res.*, *117*, B01302, doi:10.1029/2011JB008524.

Hayes, G. P., M. W. Herman, W. D. Barnhart, K. P. Furlong, S. Riquelme, H. M. Benz, E. Bergman, S. Barrientos, P. S. Earle, and S. Samsonov (2014), Continuing megathrust earthquake potential in Chile after the 2014 Iquique earthquake, *Nature*, *512*(7514), 295–298.

Hicks, S. P., A. Rietbrock, C. A. Haberland, I. Ryder, M. Simons, and A. Tassara (2012), The 2010 Mw 8.8 Maule, Chile earthquake: Nucleation and rupture propagation controlled by a subducted topographic high, *Geophys. Res. Lett.*, 39, L19308, doi:10.1029/2012GL053184.

Husen, S., E. Kissling, and E. R. Flueh (2000), Local earthquake tomography of shallow subduction in north Chile: A combined onshore and offshore study, *J. Geophys. Res.*, *105*(B12), 28,183–28,198, doi:10.1029/2000JB900229.

Kato, A., and S. Nakagawa (2014), Multiple slow-slip events during a foreshock sequence of the 2014 Iquique, Chile Mw 8.1 earthquake, *Geophys. Res. Lett.*, *41*, 5420–5427, doi:10.1002/2014GL061138.

Meng, L., H. Huang, R. Bürgmann, J. P. Ampuero, and A. Strader (2015), Dual megathrust slip behaviors of the 2014 Iquique earthquake sequence, *Earth Planet. Sci. Lett.*, *411*, 177–187.

Moreno, M., C. Haberland, O. Oncken, A. Rietbrock, S. Angiboust, and O. Heidbach (2014), Locking of the Chile subduction zone controlled by fluid pressure before the 2010 earthquake, *Nat. Geosci.*, 292–296, doi:10.1038/ngeo2102.

Okada, Y. (1985), Surface deformation due to shear and tensile faults in a half-space, *Bull. Seismol. Soc. Am.*, *75*(4), 1135–1154.

Ruiz, S., M. Metois, A. Fuenzalida, J. Ruiz, F. Leyton, R. Grandin, C. Vigny, R. Madariaga, and J. Campos (2014), Intense foreshocks and a slow slip event preceded the 2014 Iquique Mw 8.1 earthquake, *Science*, *345*(6201), 1165–1169.

Schurr, B., et al. (2014), Gradual unlocking of plate boundary controlled initiation of the 2014 Iquique earthquake, *Nature*, *512*(7514), 299–302.

Simons, M., J. E. Galetzka, J. F Genrich, F. Ortega, D. Comte, B. Glass, G. Gonzales, and E. Norabuena (2010), Central Andean Tectonic Observatory Geodetic Array, UNAVCO, GPS Data Set, doi:10.7283/T50P0X37.

Strasser, F. O., M. C. Arango, and J. J. Bommer (2010), Scaling of the source dimensions of interface and intraslab subduction-zone earthquakes with moment magnitude, *Seismol. Res. Lett.*, *81*(6), 941–950.

Tassara, A., and A. Echaurren (2012), Anatomy of the Andean subduction zone: Three-dimensional density model upgraded and compared against global-scale models, *Geophys. J. Int.*, *189*(1), 161–168.

Wdowinski, S., Y. Bock, J. Zhang, P. Fang, and J. Genrich (1997), Southern California Permanent GPS Geodetic Array: Spatial filtering of daily positions for estimating coseismic and postseismic displacements induced by the 1992 Landers earthquake, *J. Geophys. Res.*, *102*, 57–70, doi:10.1029/96JA01273.